Distributed balanced photodetectors for high-performance RF photonic systems

M. Saif Islam, Tai B. Chau, and Ming C. Wu*

Electrical Engineering Department, , University of California, Los Angeles,
Los Angeles, CA 90095-1594

Deborah L. Sivco, and Alfred Y. Cho

Lucent Technologies, Bell Laboratories, Murray Hill, NJ 07974

ABSTRACT

A novel velocity-matched distributed *balanced* photodetector operating at 1.3 and 1.55μm wavelengths has been experimentally demonstrated. Distributed absorption and velocity matching of the optical and microwave signals are employed to achieve high saturation photocurrent. A common mode rejection ratio greater than 27 dB has been achieved over a wide range of photocurrents. More than 24dB suppression of the relative intensity noise of the laser source and EDFA added noise has been achieved in a broadband RF link experiment. Shot noise limited performance has been achieved with significant improvements in the signal-to-noise ratio.

Keywords: RF photonics, noise suppression, analog fiber optic links, balanced photodetectors, optical receivers

1. INTRODUCTION

In analog fiber optic link, high speed photodetectors with high saturation photocurrent can improve the overall link performance. In externally modulated links, the link gain, noise figure, and spurious free dynamic range (SFDR) improve with increasing optical power of the link.[1] If the photodetectors have sufficiently high saturation power, this improvement will be limited by the relative intensity noise (RIN) of the laser source and the amplified spontaneous emission noise (ASE) from erbium-doped fiber amplifiers (EDFA). It is known that the laser RIN and EDFA-added noise can be suppressed by balanced receivers.[1-2] Therefore, balanced receiver with linear photocurrent under high input power is a critical component of high-performance analog fiber optic links.[2-4] High power balanced receivers are also important for optical heterodyned receivers and optoelectronic generation of high power microwaves and millimeter-waves.

Discrete balanced photodetectors with high saturation power have been reported, however, they have limited bandwidth.[5] It is also more difficult to match the electrical and optical characteristics of the photodetector pair using discrete components. Most of the reported integrated balanced receivers suffer from low saturation power and are not suitable for analog links.[6-8] Several previous works aimed at simultaneously achieving high power and high bandwidths in photodetectors using waveguide[9-10], travelling wave[11] and travelling-wave hybrid detector arrays.[12] Previously, Lin *et. al.* reported a GaAs-based velocity-matched distributed photodetector (VMDP) with a peak saturation photocurrent of 56 mA and a 3-dB bandwidth of 49 GHz.[13] Recently, InP-based long wavelength VMDP has also been reported.[14] Compared with other photodetector structures, the VMDP is more suitable for implementing balanced photodetection since it has separate optical and microwave waveguides. In this paper, we discuss the design; fabrication and system performance of a novel monolithic distributed balanced photodetector that can simultaneously achieve high saturation photocurrent and large bandwidth. A common mode rejection ratio of 27 dB and a noise suppression of 24 dB have been experimentally demonstrated.

2. THEORY AND DESIGN

The schematic drawing of the distributed balanced photodetectors is shown in Figure 1. It consists of two input optical waveguides, two arrays of high-speed metal-semiconductor-metal (MSM) photodiodes distributed along the optical

* Correspondence: Email:wu@ee.ucla.edu; URL:www.photonics.ucla.edu; Telephone: 310-825-6859, Fax:310-794-5513.

Part of the SPIE Conference on Terahertz and Gigahertz Photonics • Denver, Colorado • July 1999
SPIE Vol. 3795 • 0277-786X/99/$10.00

waveguides, and a 50Ω coplanar waveguide (CPW) output transmission line. The diodes are 23 μm long and 5 μm wide. The separation between photodiodes is 150 μm. The MSM fingers with 1μm width and 1μm spacing are patterned by optical lithography. The overlap of the MSM fingers is 10.5 μm. The central conductor of the CPW has a width of 55 μm and the separation between the central conductor and the ground conductors is 85 μm. Without the photodiodes, the velocity of the CPW is about 31.8% faster than the light velocity in the optical waveguide. The photodiode arrays provide periodic capacitance loading to slow down the microwave velocity. By adjusting the length and separation of photodiodes, velocity matching between the CPW and the optical waveguides is achieved. The impedance of CPW is also matched to 50Ω. The detector operates in balanced mode when a voltage bias is applied between the two ground electrodes of the CPW. The common-mode photocurrent flows directly to the bottom ground electrode while the difference photocurrent (signal) flows to the center conductor. The signal is then collected by the CPW.

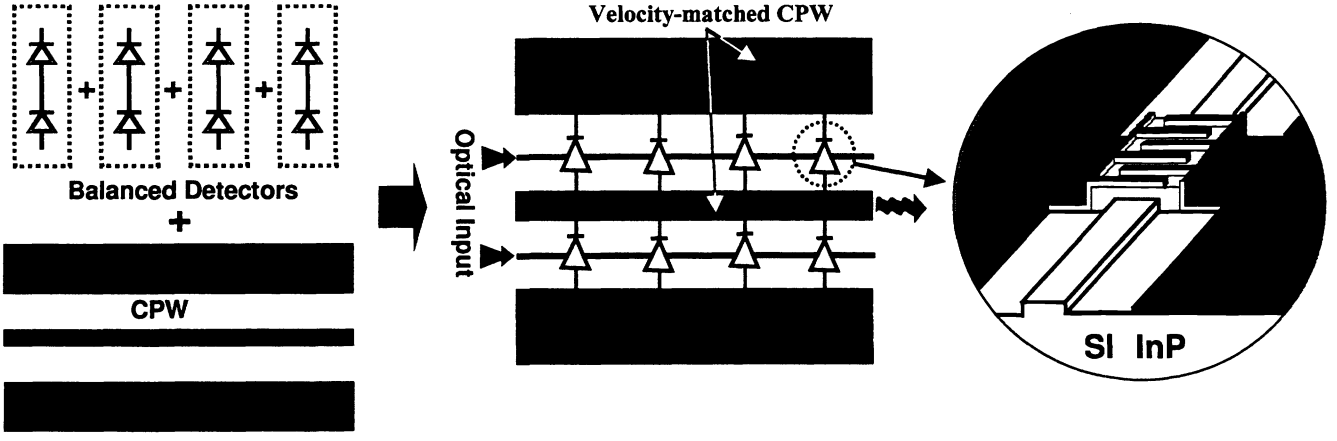

Figure 1. Principle and schematic structure of the distributed balanced photodetector. Multiple balanced photodetector pairs are cascaded in series along a coplanar waveguide to increase saturation photocurrent. The inset on the right shows the active region with an MSM photodiode. The MSM fingers provide the capacitance and resistance to the CPW and help to slow down the microwave velocity of the receiver matching it to that of optical velocity in the optical waveguide.

The distributed balanced photodetector inherits the basic advantages of the VMDP, namely, high saturation photocurrent, high quantum efficiency, and large bandwidth. It should be noted that even though only the difference current (AC signal) is collected in the balanced photodetector, the DC light is still absorbed in the photodiodes. As a result, high DC saturation photocurrent is required for the distributed balanced photodetectors. By coupling only a small fraction of light from the passive waveguide to each individual photodiodes, the photodiodes are kept below saturation even under intense optical input. Though longer absorption length is required, the bandwidth of the distributed balanced photodetector remains high because of the velocity matching. The linearity of the detector is also improved by distributed absorption because the photo carrier density is reduced in the active region.

We achieved matching of velocities and impedance using a quasi-static simulation method. A full wave analysis was later done to investigate the effects of the factors that were ignored in the quasi-static analysis. No considerable difference was observed in the performance of the balanced receiver for frequencies below 100GHz. The overall performance of the balanced receiver is determined by several factors: velocity matching, microwave loss, parasitic resistance and capacitance of the photodiode, carrier transit time in the photodiode, and coupling efficiency.

2.1. Equivalent circuit of the distributed balanced receiver

In terms of circuit elements and microwave properties, the distributed balanced photodetector resembles velocity matched distributed photodetectors (VMDP). In the receiver, a photodiode is a current source in parallel with a capacitance C_p, and then in series with a parasitic resistance R_s. We have chosen to use MSM photodiodes because of the ease of integration with the coplanar waveguide (CPW). In order to simulate the microwave performance of the receiver, we used the transmission matrix

method developed by Lin et. al.[15] The circuit equivalent of each pair of the balanced detectors in the receiver is considered in the simulation. Figure 2 depicts the equivalent circuits of the balanced photodetectors.

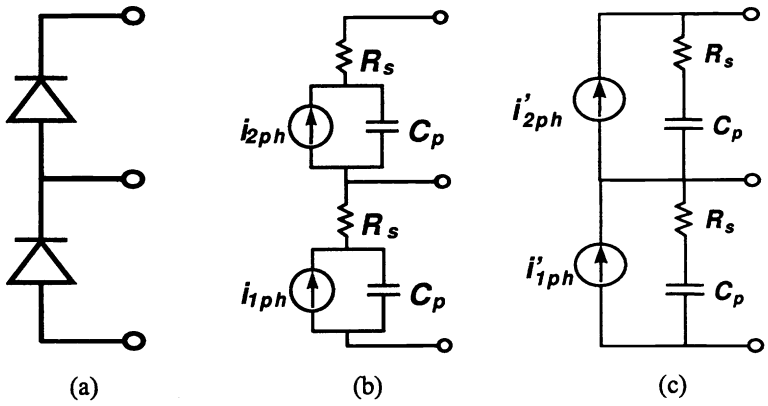

Figure 2. (a) A pair of balanced detectors (b) Equivalent circuit of the balanced detectors (c) Norton equivalent circuit of the balanced detectors.

The parameters used in the above circuit are described by the following expressions:

$$i'_{1ph} = \frac{1/j\omega C_p}{R_s + 1/j\omega C_p} i_{1ph} = \frac{1}{1 + j(\omega/\omega_c)} i_{1ph} \tag{1}$$

where $\omega_c = (R_s C_p)^{-1}$ is the RC-limited frequency of the photodiode. Similar equations can be written for i'_{2ph}. From Eq. (1), we can see that at low frequency, $i'_{1ph} \sim i_{1ph}$. As ω approaches ω_c, the magnitude of i'_{ph} decreases. The shunt inductance of the equivalent photocurrent is given by

$$Y = \frac{1}{R_s + 1/j\omega C_p} \tag{2}$$

The distributed balanced detector structure was analyzed as a microwave transmission line periodically loaded with active photodiodes, as shown in Figure 2. The equivalent circuit consists of two arrays of unit cells comprising a section of transmission line of length Δ, two shunt photodiodes admittance Y, and two current source $i'_{ph,n}$. The admittance Y and the relation between $i'_{ph,n}$ and $i_{ph,n}$ of each photodiode have been derived in Eqs. (1) and (2), respectively.

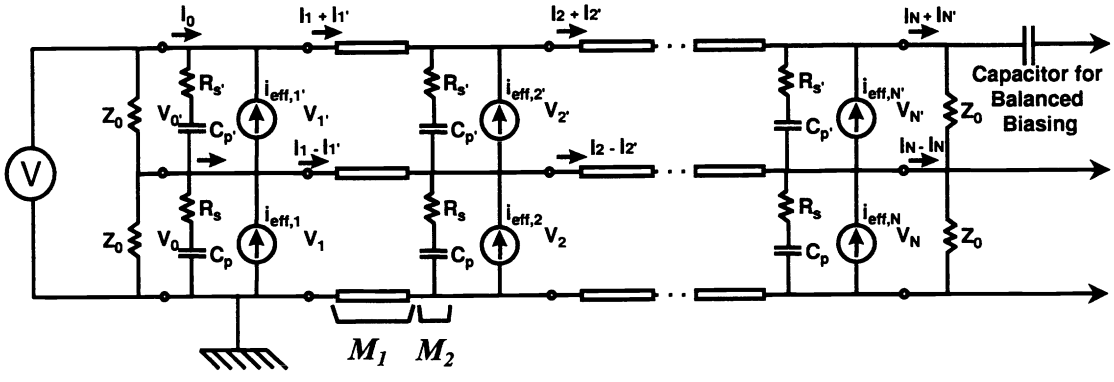

Figure 3. Equivalent circuit of the balanced receiver. In the ideal case C_p and $C_{p'}$, V_n and $V_{n'}$; $i_{eff,n}$ and $i_{eff,n'}$ and R_s and $R_{s'}$ are equal. *M1* is the transmission matrix of the transmission line segment and *M2* matrix expresses the photodiode.[16]

Following same formalism described in Ref. 15-16, which was based on Ref. 19-24, we simulated the structure to calculate the quantum efficiency, total microwave loss and other properties of the receiver. The characteristic impedance and the phase velocity of the CPW are calculated using the equivalent circuit model described in Ref. 14. The length of the photodiodes and the separation between them are adjusted to achieve simultaneous velocity matching and impedance matching. Since the separation between the central conductor and the ground electrodes (85 μm) are much smaller than the wavelength of the RF signal (about two order of magnitude smaller at 50 GHz), quasi static analysis is reasonably accurate.[17] The capacitors and resistors of each photodiodes are considered as lumped elements in our quasi-static simulation. After optimizing the receiver structure, a full-wave analysis was performed to verify the design. We found that the quasi-static results agree very well with the full wave analysis for frequency below 100 GHz. The period in our device corresponds to a cut-off frequency of 300 GHz, well above our expected frequency of operation. Therefore, the dispersion due to the periodicity of the structure is negligible for frequencies below 100 GHz.[18]

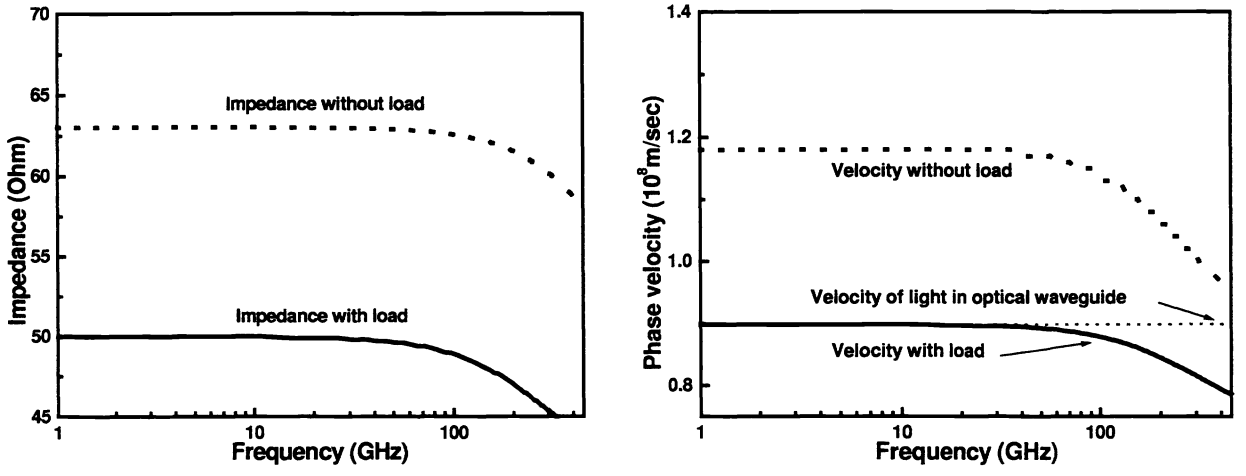

(a) (b)

Figure 4. (a) Characteristic impedance of the unloaded and periodically loaded CPW versus the microwave frequency. (b) Phase velocity of the periodically loaded CPW in the distributed balanced receiver structure, compared with the velocity of the optical wave.

2.2. Effect of periodic loading

For the distributed balanced receiver, the transmission line is periodically loaded with active photodiodes. For low frequency region where the spacing between the photodiodes is small compared to the wavelength (150 μm in our design), the effect of periodic loading on the phase velocity of microwave is given by Ref. 25:

$$v_L(f) = \left(\sqrt{\left(C_M(f) + \frac{C_{p,eq}}{\Delta} \right) \cdot L_M(f)} \right)^{-1} \tag{3}$$

where $C_M(f)$ is the equivalent capacitance and $L_M(f)$ is the equivalent inductance per unit length of the transmission line. In Eq. (3), $C_{p,eq}$ is the effective capacitance of the photodiode which is derived by taking into account both the contributions from the parasitic resistance R_s and capacitance C_p of the photodiode:

$$\frac{1}{C_{p,eq}} = \frac{1}{C_p} + j\omega R_s \tag{4}$$

The impedance of the periodically loaded transmission line can be derived under the same assumption:[25]

$$Z_L(f) = \sqrt{\frac{L_M(f)}{C_M(f) + \frac{C_{p,eq}}{\Delta}}} \tag{5}$$

We can calculate the parasitic capacitance and resistance of the MSM photodiode by using by using the method described in Ref. 26. In our structure, the MSM finger pattern has the following geometry: metal line width = 1.0 μm, finger pitch = 2.0 μm, metal thickness = 2000 Å, finger length = 18 μm, overlap finger length between electrodes = 10.5 μm, and the distance between adjacent active photodiodes is 150μm. These parameters resulted in an R_s of 1.53Ω and a C_p of 14.32fF from each photodiode in the balanced receiver. Using these parameters and the equations described in this section, the impedance and the phase velocity of the loaded transmission line in balanced receiver structure versus the frequency are plotted in Figure 4-a and 4-b, respectively. The velocity of optical wave in balanced receiver obtained from the effective refractive index of the optical waveguide is also shown in Figure 4-b.

2.3. Optical waveguide

The optical waveguide consists of the following: a 200-nm-thick $In_{0.52}Al_{0.37}Ga_{0.11}As$ lower cladding layer, a 500-nm-thick $In_{0.52}Al_{0.178}Ga_{0.302}As$ core region, a 200-nm-thick $In_{0.52}Al_{0.37}Ga_{0.11}As$ first upper cladding layer, and a thin $In_{0.52}Al_{0.48}As$ second upper cladding layer. The 150-nm-thick absorption region is located on top of the waveguide for evanescent coupling. Since the Schottky barrier height of most metals on InGaAs is typically between 0.2-0.3 eV, an $In_{0.52}Al_{0.48}As$ cap layer is used to increase the Schottky barrier height and therefore decrease the dark current of the photodiodes.[26, 27] A graded layer is incorporated in the structure to reduce the minority carrier trapping at the InAlAs-InGaAs band edge discontinuity. Figure 5-(a) shows the epi-layer of the receiver.

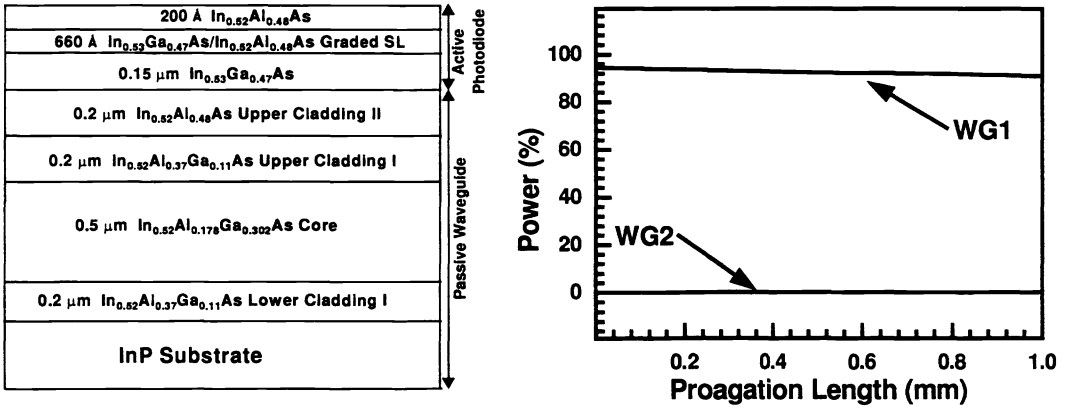

(a) (b)

Figure 5. (a) Epitaxial layer structure of the balanced receiver with active photodiode layers. (b) Optical power distribution along the waveguides when one waveguide is illuminated. No active region is considered in this simulation.

A scalar three-dimensional beam propagation method (BPM) was used to simulate the optical properties of the balanced VMDP. Our simulation shows that an AC quantum efficiency of 42% can be achieved for balanced receiver with 10 pairs of photodiodes. Since the two optical waveguides are 140 μm apart, no optical coupling between the waveguides is expected. This is confirmed by the BPM simulation. Figure 5-b shows the optical intensity profile and the power distribution along the waveguides when a fundamental mode is launched into the first waveguide (WG1) at the input. The waveguide powers were calculated using computational windows surrounding the individual waveguides. Indeed, no power coupling to

WG2 is observed in the simulation. Experimentally no response was observed in the un-illuminated VMDP when one VMDP of the receiver was illuminated. The slight decay in WG1 (0.195 dB/mm) is attributed to loss to slab mode.

The effective index in the photodiode region has an imaginary part because of the absorption of optical wave. The effective index N_{eff}, calculated using the program developed by Ref. 13 and 14, for the optical waveguide is 3.337. The group velocity of the optical wave can therefore be determined using the following equation:

$$v_{opt} = \frac{c}{N_{eff}} = 8.615 \times 10^9 \ (\text{cm/sec}) \tag{6}$$

2.4. Overall performance of the distributed balanced receiver

The overall performance of the balanced VMDP is simulated using the model in Ref. 14, which includes the transit-time frequency response of the photodiodes, the loss and dispersion of the microwave transmission line, the optical coupling loss between the photodiodes, and the residue velocity mismatch between the CPW and the optical waveguides. The length of each MSM photodiode is 23 μm, and the spacing between active photodiodes is 150 μm. The maximum quantum efficiency of 43 % is limited by the 50 Ω-matched input termination assumption (50 % of photocurrent propagates in the opposite direction of the light and is absorbed by the terminated input end) and the coupling loss between the active and passive waveguide regions. The coupling efficiency from the lensed fiber is not taken into account in this simulation since it varies with different lensed fiber tip design. The bandwidth of the VMDP with one MSM photodiode is basically the same as that of the conventional high speed MSM photodetector,[28] and can be as high as several hundred GHz, though the quantum efficiency is low because of the high power design. The simulation results are shown in Figure 6.

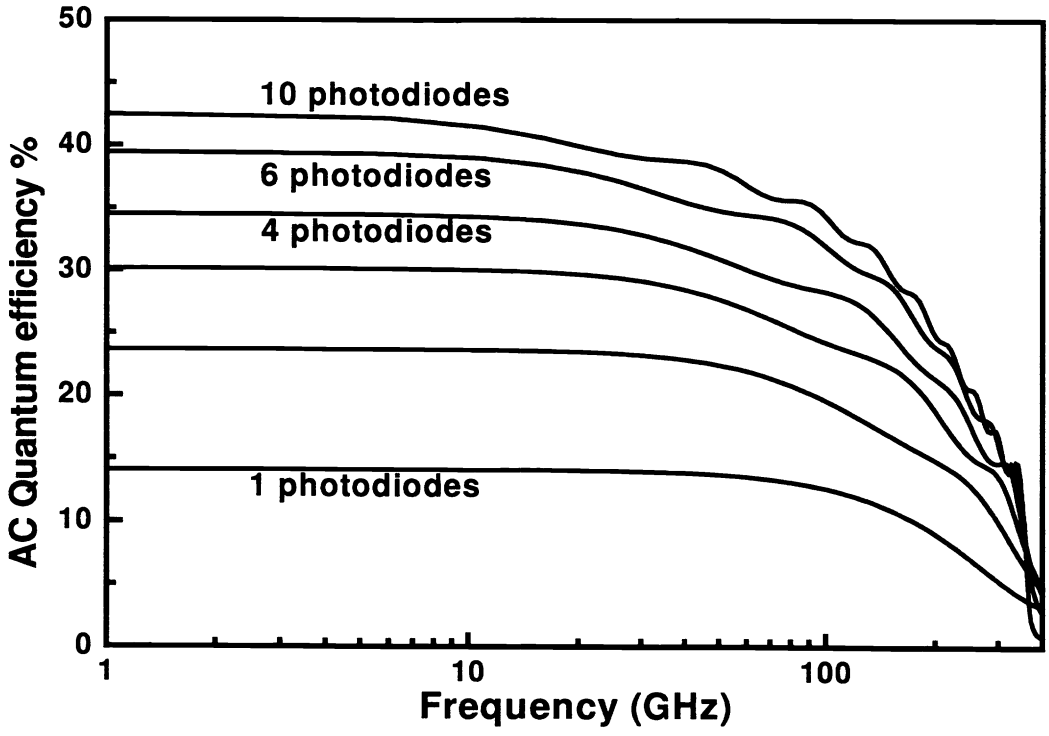

Figure 6. Simulated frequency responses of the distributed balanced receiver structure with different number of photodiode pairs. Simulation considers input end termination

3. FABRICATION

Fabrication of the receiver started with a mesa isolation step. This was done by etching away the active photodiode layers from the sample except the places where photodiodes are located. The mesa etching was performed in two steps. At first phosphoric acid based etchant (H_3PO_4, H_2O_2 and H_2O in a ratio of 1:8:60) was used to remove the InAlAs barrier enhancement layer, graded superlattice layers and half of the absorbing active InGaAs layer. The second phase of the mesa etching was performed with a selective etchant with the same mask used in the first step. Citric acid and H_2O_2 were used in 1:2 ratio. The etchant etches InGaAs active layer without etching InAlAs upper cladding II layer. We allowed the samples to remain in the solution for extra 30 seconds to cause a mushroom like profile in the mesa structure. Waveguide etching was performed with a different mask that protects the mesas and generates the waveguide patterns. We etched 0.1μm deep to fabricate a 3μm wide single mode waveguide.

A thin PECVD Si_3N_4 film of 1500Å thickness was then deposited all over sample to achieve three purposes. First, it covers the mesa walls and thus prevents the metal fingers from touching the InGaAs layer, which causes a very low Schottky barrier and high dark currents. Second, it passivates the surface of the wafer and and protects it from the atmosphere. And finally the finger tips of the MSM photodiodes and the CPW are placed op top of the dielectric layers so that soft breakdown can be prevented and dark current contributions from the CPW can be eliminated.[29]

Metal was deposited to make the MSM diodes over the top InAlAs layer of the structure. To ensure the continuity of the MSM fingers over the 0.32 μm mesa height, we used a metal thickness of 0.22μm in the MSM fingers with a combination of 200Å of Ti and 2000Å of Au. The fingers run all the way down to the CPW on the silicon nitride layer and makes Schottky contact with the InAlAs barrier enhancement layer on top of the active mesas. O_2 RIE is used to remove all residual photoresist from the exposed areas of the sample. Immediately before the metal evaporation, the sample is treated twice with 4% HF to make sure that no oxide layer degrades the Schottky contact. The process was completed by the fabrication of a coplanar waveguide (CPW) on top of the dielectric film layer. Gold was the major component of the interconnect metal although Ti was first used for adhesion.

4. MEASUREMENTS

4.1. DC measurements

The device exhibits excellent electrical and optical characteristics. The dark current is measured to be 28 $\mu A/cm^2$ at 10 V bias; the lowest reported for InAlAs/InGaAs MSM photodiodes (Figure 8-a). At the operating voltage of 4 V, the total dark current of a balanced receiver with 5 pairs of photodiodes is 1.5 nA. A pair of lensed fibers was used to couple light into the photodetector. The devices are usually biased at 4 V for quantum efficiency, frequency response, and saturation photocurrent measurement. Since there is dielectric isolation between the semiconductor and the coplanar waveguide lines, the leakage could be kept to a very low level.

By coupling light directly from a lensed fiber and testing 15 devices, the average DC responsivity was measured to be 0.45A/W at 8V bias. Higher responsivity such as 0.6A/W has been observed in some devices. The photo response of a laser beam with TM polarization is measured to be ~1.7 dB higher than that of TE polarization. The coupling efficiency of the lensed fibers in our setup was calculated to be ~50%. With antireflection (AR) coating to the balanced receiver facet (30% Fresnel loss), the average responsivity can be increased to 0.64A/W. The responsivity can be further improved by optimizing the coupling efficiency of the lensed fiber as well as reducing the coupling loss between the passive and active waveguide regions by better control of the etching steps during the fabrication.

In section two, it was discussed how the VMDP based balanced receiver is likely to reach very high power level without losing the bandwidth of individual photodiodes in the receiver. When a good waveguide distributes almost equal amount of optical power to each photodiode, the saturation power is increased. Our receiver was found to be linear with a total DC photocurrent of 12mA (Figure 7-b). Most of these photocurrents are generated in the first pair of photodiodes as the waveguide of our first design has high optical loss between the waveguides and the active photodiode sections. We are currently working on the optimization of the waveguide structure by using straight multimode waveguides.[30] A distributed balanced receiver with optimized waveguides is likely to go above 100mA of photocurrent at very high bandwidths.

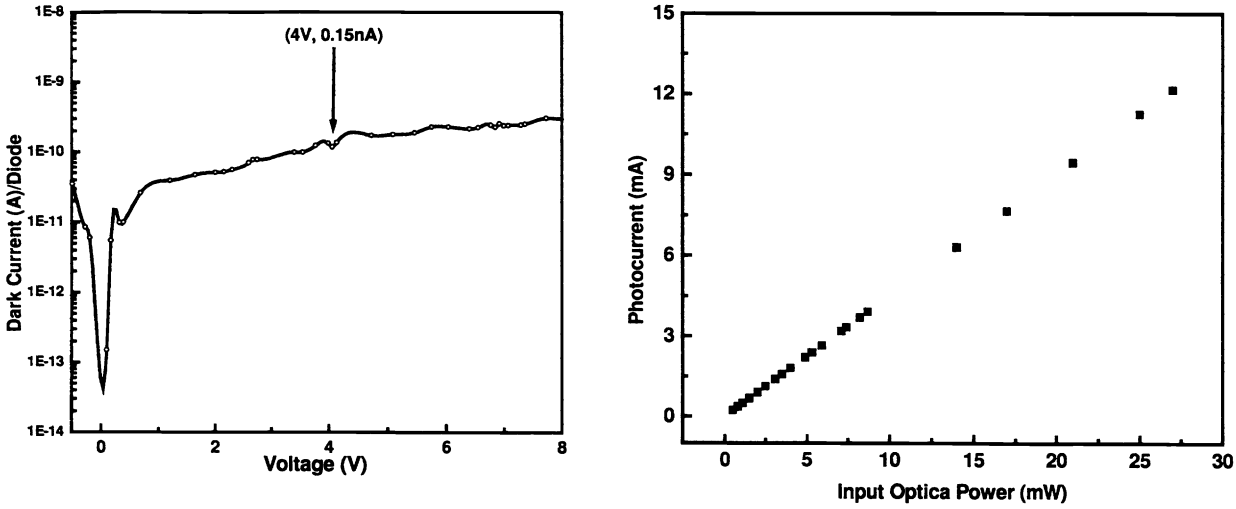

(a) (b)

Figure 7. (a) The dark current versus bias voltage for individual VMDP (one array of photodiodes) in the balanced detector. At the operational bias (4 V), the dark current contribution from each MSM diode is ~0.15 nA. (b) DC photocurrent versus input optical power (without AR coating). (b) The DC photocurrent remains linear up to 12 mA for each branch of the balanced receiver, which makes a total linear photocurrent of 24mA.

All the characteristics of the photodiodes in our monolithic balanced detectors are identical. This resulted in a very good common mode rejection ratio (CMRR). Very high CMRR (> 27 dB) is measured for a wide range of photocurrent from 30 nA to 12 mA. Figure 8-a plots the CMRR of a typical VMDP in the balanced receiver.

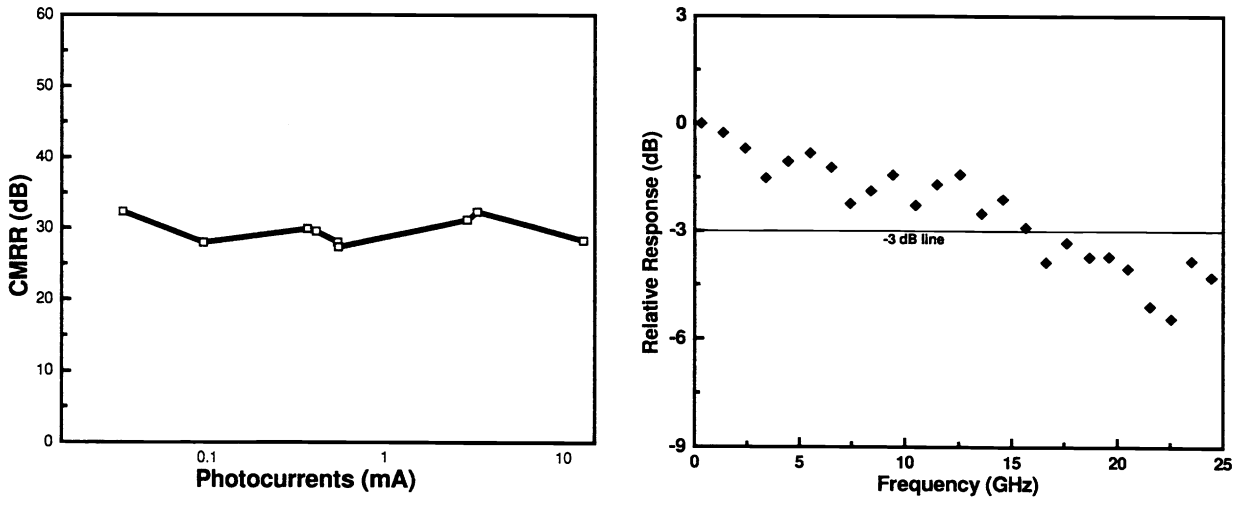

(a) (b)

Figure 8. (a) Common mode rejection ratio (CMRR) versus photocurrent for the distributed balanced receiver. The high CMRR results from the closely matched photodiode characteristics in our monolithic device. (b) Frequency response of the distributed balanced photodetector illuminating only one waveguide at a time.

4.2. RF measurements

4.2.1. Frequency response

The frequency response of the balanced VMDP was first characterized with light coupled to one waveguide only. Using the optical heterodyne technique with two external cavity tunable semiconductor lasers at 1.55 μm, the 3-dB bandwidth was found to be 16 GHz for both photodetector arrays. The frequency response of the microwave cable, splitter, amplifier, bias-T, and probe are separately characterized up to 50 GHz by HP 8510C network analyzer. The overall and calibrated frequency response is shown in Figure 8-b. The bandwidth is currently limited by the carrier transit time of the MSM photodiodes. Since the bandwidth of our capacitance loaded CPW is much greater than 40 GHz, the bandwidth of the balanced VMDP can be increased by scaling down the MSM photodiodes. Theoretical simulation indicates that bandwidth > 100 GHz is achievable.

4.2.2. Impedance of the microwave transmission line

A HP 8510C network analyzer was used to measure the characteristic impedance and the microwave return loss (S_{11}) of the balanced receiver. Two-port measurement for transmission lines was employed. The probes and microwave connections on both ports are calibrated using the standard calibration patterns for the picoprobes from GGB industry, including short, open, and 50 Ω–through transmission line. By measuring the reflection coefficient from one port, the impedance of the transmission line can be determined. Figure 9 shows the measured S parameters of the receiver. The S_{11} is below -30 dB from 45 MHz to 40 GHz, indicating that the impedance of the detector is very well matched to 50 Ω. The loaded CPW has very low insertion loss. The measured S_{12} shows a drop of only 0.6 dB from 45 MHz to 40 GHz.

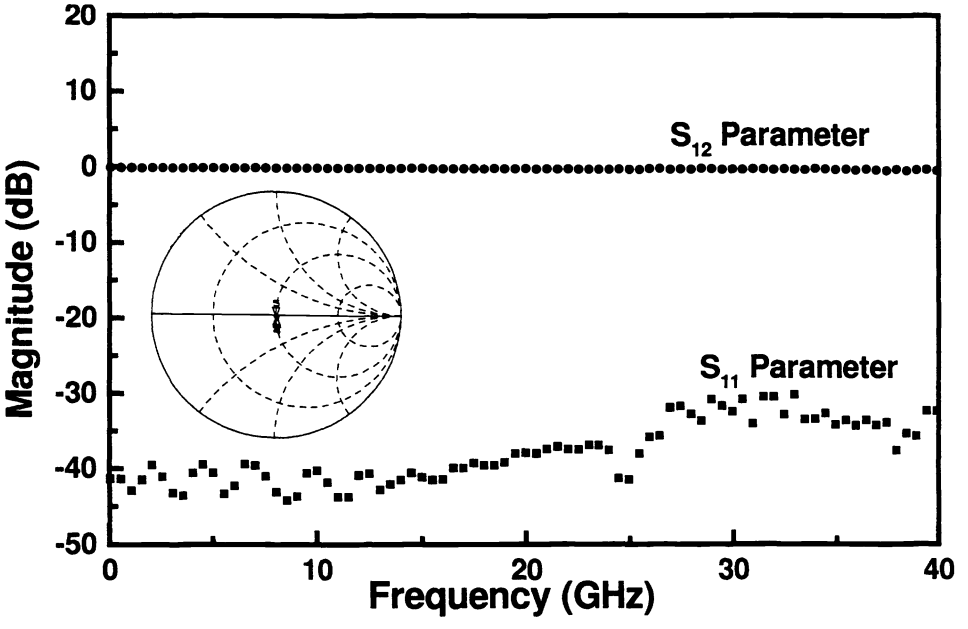

Figure 9. S_{22} measurement of the transmission line using HP 8510C network analyzer. The Smith chart in the inset generated by the network analyzer shows the impedance matching to 50 Ω.

4.3. Balanced detection experiment

Figure 10 depicts the experimental setup for balanced detection. A distributed feedback (DFB) laser with 1542-nm wavelength and 0 dBm output power is employed as optical source. It is amplified by an EDFA and then filtered by an optical bandpass filter with 2-nm bandwidth. The microwave signal was modulated onto the optical carrier by an X-coupled Mach-Zehnder modulator (MZM), which produces two complimentary outputs for the balanced VMDP. The outputs are coupled to the balanced VMDP by two lensed fibers. To maximize the signal enhancement and noise cancellation, it is important to match the

amplitudes and phases of the two detected microwave signals. In our experiment, a variable attenuator was used to match the amplitudes of the photocurrents.

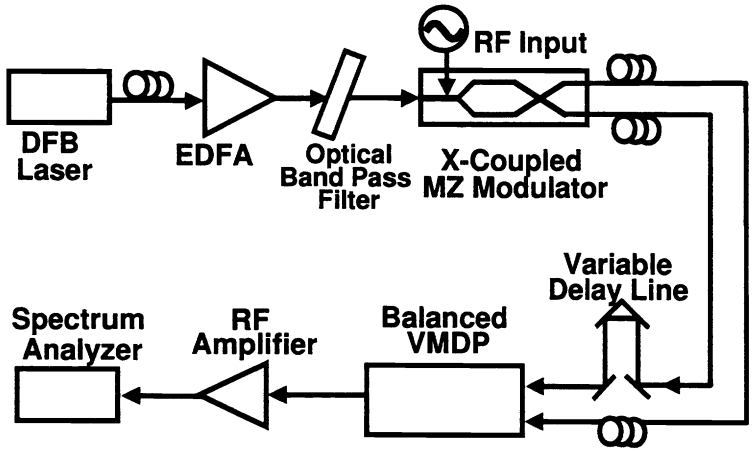

Figure 10. Experimental setup for balanced detection. The complimentary input signals are produced by the X-coupled MZ modulator.

Typical balance between the VMDP was within 2% of the total photocurrent reading. We also employed a variable optical delay line to match the path lengths of both the MZM outputs that go to the receiver. For balanced detection, the RF signals need to be exactly 180° out of phase. When path lengths are equal, the signals are always in 180° phase difference for all microwave frequencies.

4.3.1. Balanced biasing

Balanced detection is achieved by applying a bias of 8 V between the two ground electrodes of the CPW. A custom-made high-frequency probe with an integrated DC-blocking capacitor on one ground probe is used to collect the microwave output signal. The DC photocurrents are measured through two ammeters: the difference photocurrent (i_{DIFF}) is monitored through the bias-T connected to the probe, and the common mode photocurrent (i_{COM}) is monitored between the ground electrodes of the CPW. Figure 11-a depicts the biasing circuit in balanced mode.

To verify the balanced detection, we modulated the optical input at 5 and 8 GHz and varied the delay of the fiber optic delay line from 0 to 50 mm. Figure 12-b shows the detected RF signal versus the delay. When the received RF signals have a 0° phase difference, the RF output is cancelled out in balanced mode. When the detected RF signals are 180° out of phase, the small signal photocurrents from the two photodiode arrays are added in phase and maximum RF signal is observed. The extinction ratio is more than 44 dB.

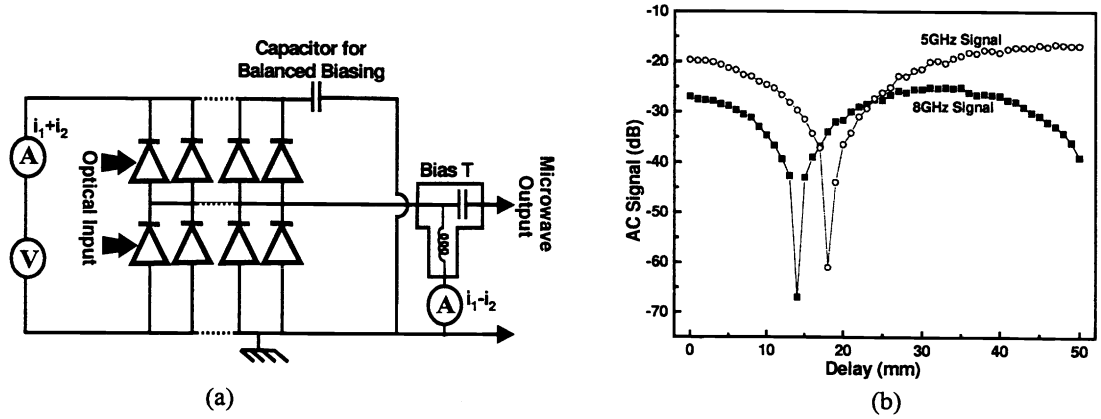

Figure 11 (a) The biasing circuit for balanced detection. (b) The peak RF power detected in the balanced mode versus the time delay of one input light. Periodic variation is observed. The period is measured to be 38.75 mm at 8 GHz RF signal, which is very close to the calculated value. For the 5 GHz signal, period is ~60mm. The Extinction ratio is greater than 44 dB.

4.3.2. Laser RIN suppression

One key advantage of the balanced photodetector is its ability to cancel out the laser RIN. To evaluate the cancellation ratio of our device, we compare the noise spectra of a DFB laser measured by our photodetector in the unbalanced and the balanced modes. The DFB laser operates in CW condition and has a RIN peak at 4.16 GHz. Figure 12-b shows the noise spectra measured near its RIN peak when only one waveguide is illuminated. We confirm that the noise is dominated by the RIN of the DFB laser and the EDFA added noise. When the optical input power is doubled, the noise floor increases by 6 dB. We then biased the photodetector in the balanced mode and coupled the input to both the optical waveguides. The bottom trace in Figure 12-a shows the noise spectra detected by the balanced detector. Suppression of the RIN by as much as 36 dB is observed. The maximum suppression occurs at 4.16 GHz, at which frequency the RIN is dominant. By setting the path length to equal value, we thus achieved broadband noise suppression with our device. Except at the relaxation oscillation frequency of the laser at which the RIN is very high (4.16 GHz), the receiver suppresses noise by more than 36dB and reaches the calculated shot noise floor.

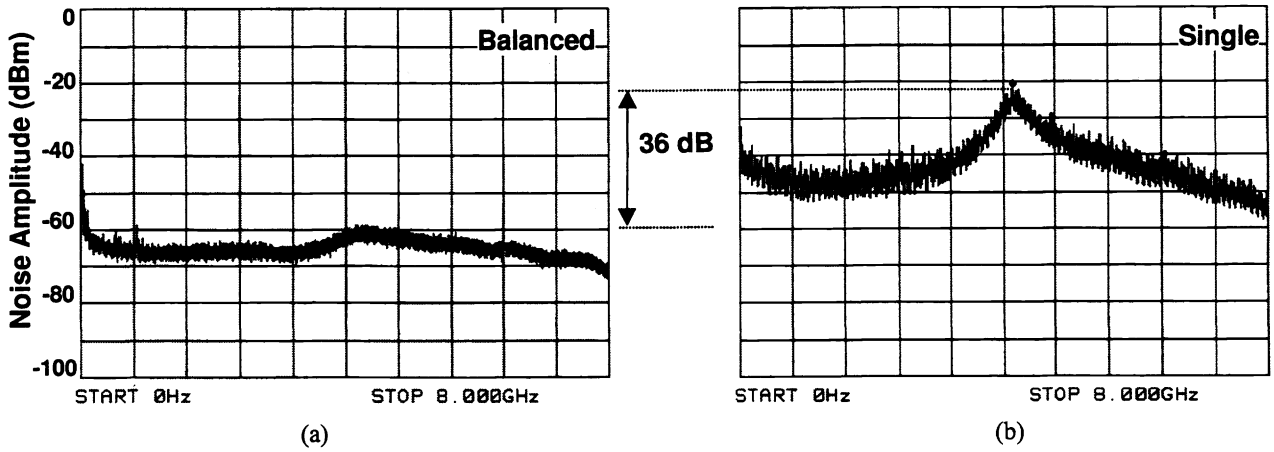

Figure 12. The noise spectra of a DFB laser measured by the distributed balanced photodetector in unbalanced mode (right trace) and balanced mode (left trace). Other than some frequencies where RIN is very high, the receiver suppresses noise by more than 36dB and reaches the shot noise floor.

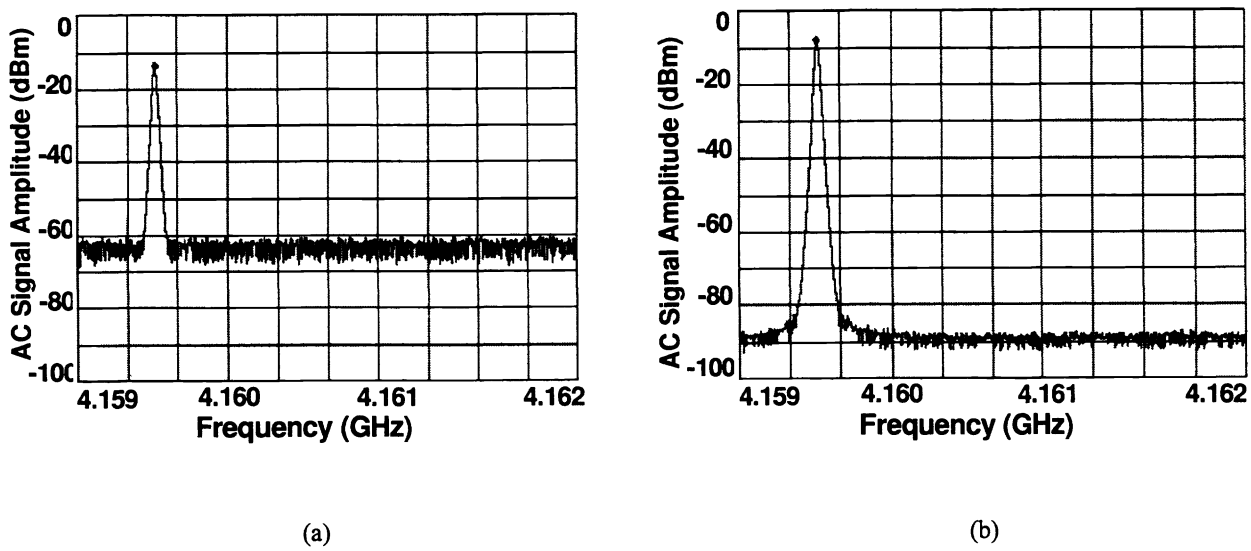

Figure 13. The RF spectra of the modulated signal detected in (a) unbalanced and (b) balanced mode. The peak of the balanced output is 6-dB higher than that of the unbalanced signal. Noise suppression in excess of 24-dB is achieved.

Figure 13 shows the RF spectra of the output from the balanced VMDP in the unbalanced (only one waveguide is illuminated) and the balanced mode. Suppression of the noise floor by 24 dB has been observed in the balanced mode over a wide frequency range from MHz to 15 GHz. This is equivalent to 27 dB improvement of noise if two outputs were considered. The signal is also enhanced by 6 dB. Different magnitudes of noise suppression were observed over a wide frequency range up to 11 GHz. Figure 14-a plots the total amount of noise cancelled versus frequency. For the upper curve the DFB was biased at 23.1 mA and was found to have very high RIN noise (shown in Figure 12-b). The lower curve is for a bias of 31mA current. In both cases the receiver reaches the calculated shot noise floor by canceling the RIN in the carrier.

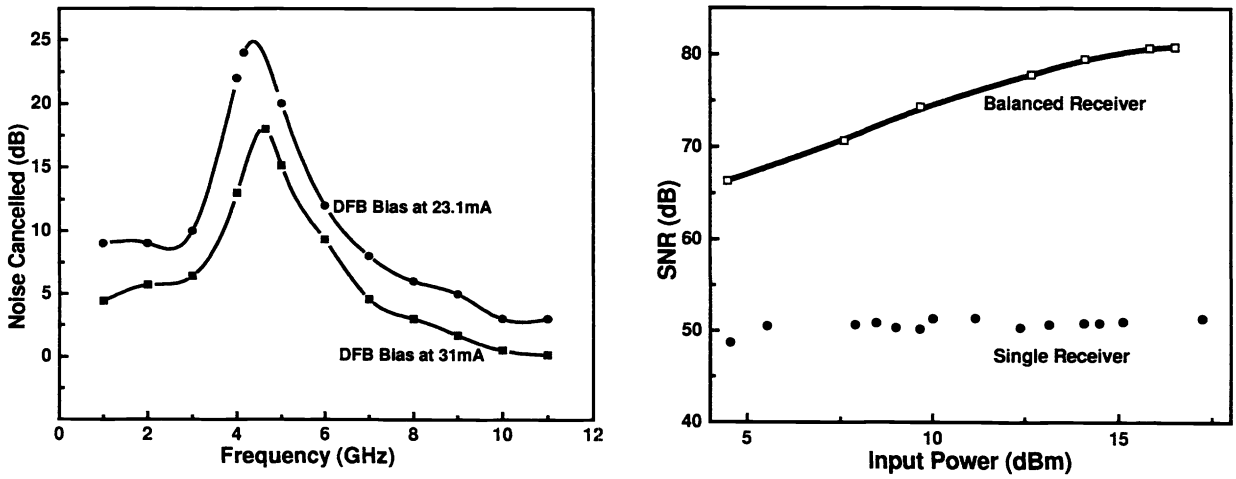

(a) (b)

Figure 14. (a) Total amount of suppressed noise at different frequencies is plotted for two different DFB bias currents. In both cases, RIN is suppressed below the shot noise floor. (b) Measured signal-to-noise ratio (SNR) of the balanced receiver. The data points in the lower half of the graph shows the SNR for the receiver in unbalanced (single input) configuration.

4.3.3. Signal-to-noise ratio (SNR)

Figure 14 (b) shows the SNR of the link versus the received optical power for both the distributed balanced receiver and the reference receiver with a single detector. The SNR for the single detector receiver is almost constant with increasing optical power, indicating that the receiver noise is dominated by the RIN. In contrast, the SNR for the balanced receiver increases monotonically with optical power upto 15 mW. For optical power greater than 15 mW, the SNR still increases monotonically with optical power at a smaller rate. This suggests the presence of some residue RIN. Comparing the two receivers, it is also noted that the SNR for the balanced receiver is 23 dB higher than that of a single detector receiver.

4.3.4. Tolerance in phase matching

The RF signals detected by the balanced detector should be exactly at 180° out of phase for optimum noise suppression. This requires the lengths of the fiber from the complimentary MZM to the detector to be exactly the same in length. In practical applications, the optical path length will drift slightly due to environmental changes and it is important to understand the impact of phase mismatch. We intentionally allowed the signals to have different phase differences and investigated the magnitude noise suppression and signal peak variations. The measured data shows that even with a phase variation of 100°, our device can suppress more than 9 dB of RIN noise whereas the signal peak reduction was less than 4 dB.[31] As balanced detector amplifies the RF signal by 6dB, with a phase deviation of 100°, the signal is still higher than that of an unbalanced detector. For the RF signal at 6.5 GHz, 100° phase variation between two fibers corresponds to ~8.5mm of fiber length.

5. CONCLUSION

We have successfully designed, fabricated, and experimentally demonstrated a balanced velocity-matched distributed photodetector (VMDP) with both impedance and velocity matching. The velocity matching between the incident optical wave and the output microwave signal allows the detector length and effective absorption volume to increase without penalizing the bandwidth. Therefore, high saturation power and high speed are achieved simultaneously. The device exhibits a very low dark current (1.5 nA for the balanced VMDP with 5 pairs of photodiodes) and a high external quantum efficiency (0.64 A/W). The relative intensity noise (RIN) of a semiconductor distributed feedback laser has been suppressed by 24 dB, and the RF signal has been enhanced by 6 dB.

Our future works includes deep waveguide etching to efficiently guide the input light in the waveguide and effectively distribute light to all the photodiodes in the receiver. This is expected to improve the DC and AC linearity at high photocurrent levels. In the long run, we plan to test the performance of the high power balanced receiver in various potential fiber optic systems.

6. ACKNOWLEDGEMENT

The authors would like to acknowledge Prof. T. Itoh of UCLA for helpful discussions; Dr. D.T.K. Tong of Lucent Technologies-Bell Laboratories, Homedel NJ, for his helpful suggestions about the experimental setup, members of High-speed Optoelectronics Technology group of Integrated Photonics Laboratory at UCLA for their cooperation in the design and characterization of the device; and D. L. Sivco, and Dr. A. Y. Cho of Lucent Technologies-Bell Laboratories, Murray Hill, NJ, for their contribution in growing the wafer for the distributed balanced receiver. This project was supported by ONR MURI on RF photonics, NRAO and UC MICRO.

REFERENCES

1. N. K. J. Williams and R. D. Esman, "Optimizing the ultrawideband photonic link," *IEEE Transaction on Microwave Theory and Techniques*, vol. 45, no. 8, pp. 1384 - 1389, 1997.
2. C. H. III Cox, G. E. Betts, and L. M. Johnson, "An analytic and experimental comparison of direct and external modulation in analog fiber-optic links," *IEEE Transaction on Microwave Theory and Techniques*, vol. 38, no. 5, pp 501-509, May 1991.
3. C. H. Cox, "Analog fiber-optic links with intrinsic gain," *Microwave Journal,* Vol. 35, no. 9, p. 92-99, 1992.
4. R. F. Kalman, J. C. Fan, and L. G. Kazovsky, "Dynamic range of coherent analog fiber-optic links," *J. Lightwave Tech.,* Vol. 12, no. 7, p. 1263-1277, 1994.
5. K. J. Williams and R. D. Esman, "Optically amplified down converting link with shot-noise limited performance," *IEEE Photon. Technol. Lett.*, vol. 8, no. 1, pp. 148 - 150, 1996.
6. D. Trommer, A. Umbach, W. Passenberg and G. Unterborsch, "A monolithically integrated balanced mixer OEIC on InP for coherent receiver applications," *IEEE Photon. Technol Lett.*, vol.5, no. 9, pp.1038-40, 1993.
7. F. Ghirardi, A. Bruno, B. Mersali, J. Brandon, L. Giraudet, A. Scavennec and A. Carenco, "Monolithic integration of an InP based polarization diversity heterodyne photoreceiver with electrooptic adjustability," *Journal of Lightwave Technology*, vol.13, no. 7, pp.1536-49, 1995.
8. R.J. Deri, E.C.M. Pennings, A. Scherer, A.S. Gozdz, C. Caneau, N.C. Andreadakis, V. Shah, L. Curtis, R.J. Hawkins, J.B.D. Soole and J.-I. Song, "Ultracompact monolithic integration of balanced, polarization diversity photodetectors for coherent lightwave receivers," *IEEE Photon Technol Lett.*, vol.4, no. 11, pp.1238-40, 1992.
9. A.R. Williams, A. L. Kellner, X. S. Jiang, P. K. L.Yu, "InGaAs/InP waveguide photodetector with high saturation intensity," *Electronics Letters*, vol.28, no.24, p.2258-919, 1992.
10. S. Jasmin, N. Vodjdani, J-C. Renaud and A. Enard, "Diluted and distributed-absorption microwave waveguide photodiodes for high efficiency and high power," *IEEE Transaction on Microwave Theory and Techniques*, vol. 45, no. 8, pp. 1337 - 1341, 1997.
11. K. S. Giboney, M. J. W. Rodwell, J. E. Bowers, "Travelling-wave photodetector theory," *IEEE Transaction on Microwave Theory and Techniques*, vol. 45, no. 8, pp. 1310 - 1319, 1997.
12. C. L. Goldsmith, G. A. Magel, R. J. Boca, "Principals and performance of travelling-wave photodetector arrays," *IEEE Transaction on Microwave Theory and Techniques*, vol. 45, no. 8, pp. 1310 - 1319, 1997.

13. L. Y. Lin, M. C. Wu, T. Itoh, T. A. Vang, R. E. Muller, D. L. Sivco, and A. Y. Cho, "Velocity-matched distributed photodetectors with high-saturation power and large bandwidth," *IEEE Photon. Technol. Lett.*, vol. 8, no. 10, pp. 1376 - 1378, 1996.
14. T. Chau, L. Fan, D.T.K. Tong, S. Mathai, M.C. Wu, D.L. Sivco and A.Y. Cho, "Long Wavelength Velocity-Matched Distributed Photodetectors for RF Fibre Optic Links," *Electronics Letters*, Vol. 34, No. 14, pp. 1422-1424, July 1998.
15 L. Y. Lin, "High-Power, High-speed photodetectors and micromachined free-space integrated optics," Ph.D. dissertation, Elec. Eng. Dept. UCLA, Los Angeles, CA, 1996.
16. L. Y. Lin, M. C. Wu, T. Itoh, T. A. Vang, R. E. Muller, D. L. Sivco, and A. Y. Cho, "High-power high speed photodetectors-design, analysis, and experimental demonstration" *IEEE Transaction on Microwave Theory and Techniques*, vol. 45, no. 8, pp. 1320 - 1331, 1997.
17. M. N. Khan, A. Gopinath, J. P. G. Bristow and J. P. Donnelly, " Technique for velocity-matching traveling-wave electroopticmodulator in AlGaAs/GaAs," *IEEE Transaction on Microwave Theory and Techniques*, vol. 41, no. 2, pp. 244 - 249, 1993.
18. R. Spickermann and Nadir Dagli, "Experimental analysis of millimeter wave coplanar waveguide slow wave structure on GaAs", *IEEE Transaction on Microwave Theory and Techniques*, vol. 42, no. 10, pp. 1918 - 1924, 1994.
19. K. C. Gupta, R. Garg, and I. J. Bahl, *Microstrip Lines and Slotlines*, Ch. 7, Artech House, 1979.
20. I. J. Bahl, "Design considerations for coplanar waveguides and coplanar strips," *Tech. Rep., E.E. Dept., I.I.T., Kanpur,* Vol. 78-MW1, 1978.
21. M. E. Davis, E. W. Williams, and A. C. Celestini, "Finite-boundary corrections to the coplanar waveguide analysis," *IEEE Trans. on Microwave Theory and Tech.,*Vol. 21, no. 9, p. 594-596, 1973.
22. G. Hasnain, A. Dienes, and J. R. Whinnery, "Dispersion of picosecond pulses in coplanar transmission lines," *IEEE Trans. Microwave Theory Tech.,* Vol. 34, no. 6, p. 738-741, 1989.
23. M. Y. Frankel, S. Gupta, J. A. Valdmanis, and G. A. Mourou, "Terahertz attenuation and dispersion characteristics of coplanar transmission lines," *IEEE Trans. Microwave Theory Tech.,* Vol. 39, no. 6, p. 910-916, 1991.
24. C. P. Wen, "Coplanar waveguide: A surface strip transmission line suitable for non-reciprocal gyromagnetic device application," *IEEE Trans. Microwave Theory Tech.,* Vol. 17, p. 1087-1090, 1969.
25. R. E. Collin, *Foundations for Microwave Engineering*, 2nd ed., Ch. 8, 1992.
26. J. B. D. Soole and H. Schumacher, " InGaAs Metal-Semiconductor-Metal photodetectors for long wavelength optical communications," IEEE Journal of Quantum Electronics, vol. 27, no. 3, pp 737-752, 1991.
27. E. Sano, M. Yoneama, T. Enoki and T. Tamamura, "Performance dependance of InGaAs MSM photodetectors on barrier-enhancement layer structures," *Electron. Lett.*, vol. 28, no.13, pp 1220-1221, 1992.
28. M. C. Wu and T. Itoh, "Ultrafast photonic-to-microwave transformer (PMT)," in *IEEE LEOS Summer Topical Meeting on Optical Microwave Interactions*, Santa Barbara, CA, July 19-21, 1993.
29. W. A. Wohlmuth, P. Fay and I. Adesida, "Dark current suppression in GaAs Metal-Semiconductor-Metal photodetectors," *IEEE Photon. Technol. Lett.*, vol. 8, no. 8, pp. 1061 - 1064, 1996.
30. K. Kato, S. Hata, K. Kawano, J. Yoshida, and A. Kozen, "A high efficiency 50 GHz InGaAs multimode waveguide photodetector," *IEEE J. Quantum Electron.*, vol. 28, pp.2728-2735, 1992.
31. M. S. Islam, T. Chau, S. Mathai, T. Itoh, M. C. Wu, D. L. Sivco, and A Cho, "Distributed balanced photodetectors for broadband noise suppression," accepted for publication in *IEEE Transaction on Microwave Theory and Techniques, July 1999.*